Hybridized Radial and Edge Coupled 3D Plasmon Modes in Self-Assembled Graphene Nanocylinders

Chunhui Dai[#1], Kriti Agarwal[#1], Hans A. Bechtel[2], Chao Liu[1], Daeha Joung[1], Andrei Nemilentsau[1], Qun Su[1], Tony Low[1], Steven Koester[1], and Jeong-Hyun Cho[1*]

1. Department of Electrical and Computer Engineering, University of Minnesota, Minneapolis, Minnesota 55455, USA
2. Advanced Light Source Division, Lawrence Berkeley National Laboratory, Berkeley, 94720, California, USA

jcho@umn.edu

Abstract

Current graphene-based plasmonic devices are restricted to two-dimensional (2D) patterns defined on planar substrates; thus, they suffer from severe substrate-induced losses and spatially-limited 2D plasmon fields. Here, we introduce three-dimensional (3D) graphene forming freestanding nanocylinders realized by a plasma-triggered self-assembly process. The graphene-based nanocylinders induce hybridized edge (in-plane) and radial (out-of-plane) coupled 3D plasmon modes stemming from their curvature, resulting in a four orders of magnitude stronger field at the openings of the cylinders than in rectangular 2D graphene ribbons. For the characterization of the 3D plasmon modes, synchrotron nanospectroscopy measurements were performed, which provides the first evidence of preservation of graphene plasmons in the high precision curved 3D nanocylinders. The result clearly demonstrates a ~~two order of confinement of the incident light by the plasmons in the 3D graphene cylinders and a~~ superior ~~absorption~~ plasmon resonances at the coupled edges with a plasmon wavelength of 240 nm ~~in the nano-gap~~ within the cylindrical structures.

Keywords: graphene, nanocylinder, plasmon, 3D, self-assembly

Introduction

Current graphene-based plasmonic devices [1-5] are restricted to 2D patterns defined on planar substrates due to the intrinsic geometrical limitations of graphene's 2D form [6-11]. The limited geometry (2D configuration) induces only an edge coupled surface plasmon mode on the graphene surface (in-plane direction) [12], causing graphene to suffer from spatially-limited 2D plasmon fields with low spatial coverage of the enhanced near-field and extreme susceptibility to the underlying substrate material and edge damping [13,14]. One strategy to overcome the surface-limited fields induced by the in-plane plasmon mode is to extend graphene in the out-of-plane direction by building three-dimensional (3D) graphene structures. A large number of techniques have been explored to achieve 3D forms of graphene such as graphene-based stacks [15-17], wrinkles [18-20], and bubbles [21,22] where the additional dimension offers enhanced optical properties, as demonstrated by, for example, amplified gate tunability via distributed carriers into 3D stacked graphene layers [15]; programmable plasmon reflection by manipulating the morphology of graphene wrinkles [20]; and ultra-confined plasmonic hotspots from trapped plasmons within graphene bubbles [21]. However, these simple structures still suffer from a lack of non-spatially limited hybridized 3D plasmon modes, due to the limited coupling pathways, which exhibit low sensitivity, poor and inaccessible spatial coverage of the enhanced field (between the stack layers and inside the bubbles), and a low figure of merit (FOM). Therefore, it is necessary to design 3D structures that simultaneously induce hybridized in-plane and out-of-plane coupled 3D plasmon modes, and a technique to fabricate well-controlled 3D graphene architectures is urgently required to explore the blue ocean of 3D graphene plasmons. To explore the novel physical properties, origami inspired self-assembled

3D graphene structures have been realized [23-26] with theoretical investigation of the 3D plasmons (large surface area modes, volumetric fields, and nano focused fields based on the coupling within their geometry over an added dimensionality) induced in polyhedron [27,28]. However, the polyhedral structures sacrifice high intensity edge and locally confined in-plane modes for the bulk area and volume (out-of-plane) modes. To ~~explore the vast ocean of~~realize 3D graphene plasmonics with true volumetric plasmonic enhancement, it is necessary to retain the edge and localized modes while simultaneously achieving non-surface limited fields.

In this paper, we develop hybridized edge (in-plane) and radial (out-of-plane) coupled 3D plasmon modes by realizing 3D cylindrical graphene nanostructures (Figure 1) and investigate their 3D plasmonic behaviors (Figure 1d-f). A large array of graphene-based nanocylinders is realized using a self-assembly process that offers halfway (Figure 1b) and fully curved cylindrical (Figure 1c) graphene nanostructures suspended on a substrate. For the characterization of the 3D plasmon resonances in the cylindrical graphene, synchrotron infrared nanospectroscopy (SINS) measurements are carried out and is the first evidence of plasmon resonance in well-defined complex 3D graphene geometries. The comparative analysis of the data extracted from the ~~AFM-based IR~~ scattering-type scanning near-field optical microscopy (s-SNOM) ~~imaging~~ image and the simulated results ~~and spectral information~~ reveals ~~a confinement factor of two orders of magnitude~~the superior plasmon resonance and scattering within the 3D graphene cylinders without losses from substrate or their 3D configurations and with superior FOM compared to its 2D nanoribbons counterpart..

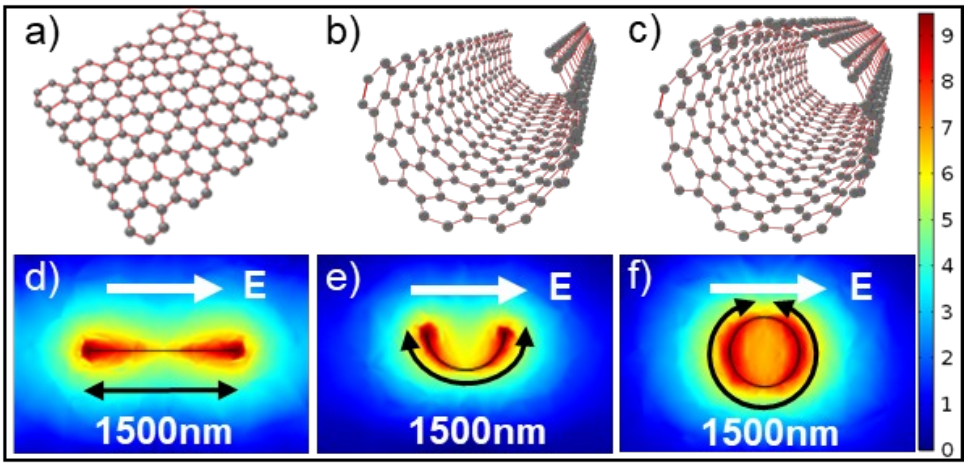

Figure 1. Schematic illustration of the transformation of a) 2D graphene ribbon, b) half-way curved graphene cylinder, and c) 3D graphene cylinders. d-f) Change in the electric field distribution simulated as a result of curving of graphene structures. The color bar shows the value of the mapped electric-field enhancement in the graphene structures in natural log scale.

An array (30×100) of 2D graphene-based ribbons [3 nm thick aluminum oxide (Al_2O_3)/single layer CVD graphene/3 nm thick Al_2O_3/5 nm tin (Sn)], each with dimensions of 1.5μm×15 μm, was first fabricated on a high resistivity silicon (Si) substrate (Figure 2a,e,i,m). In the sandwiched structure, the two layers of Al_2O_3 work as frames supporting the graphene as well as protection layers, shielding the graphene from being damaged by an etching process during self-curving. The Sn layer is the actuation layer [29], generating surface tension forces during the plasma triggered self-assembly process in a reactive ion etching (RIE) system (Figure 2a-c,) , curving the 2D graphene-based ribbons out of plane to form partially (Figure 2b,f,j,n) and, with further self-assembly time, completely curved graphene-based nanocylinders (Figure 2c,g,k,o). The Sn layer is selectively etched away in nitric acid (Figure 2d,h,l,p). A high yield (~100%) of self-curving has been achieved for 30×100 arrays (Figure 2g) where the yield is not affected by the number of arrays since the self-curving is a parallel process. Even after wet

etching of Sn, most of the samples maintain their original cylindrical shapes (Figure 2h,l,p). Only the nanocylinders that fully released from the substrate during RIE are washed away (Figure 2l).

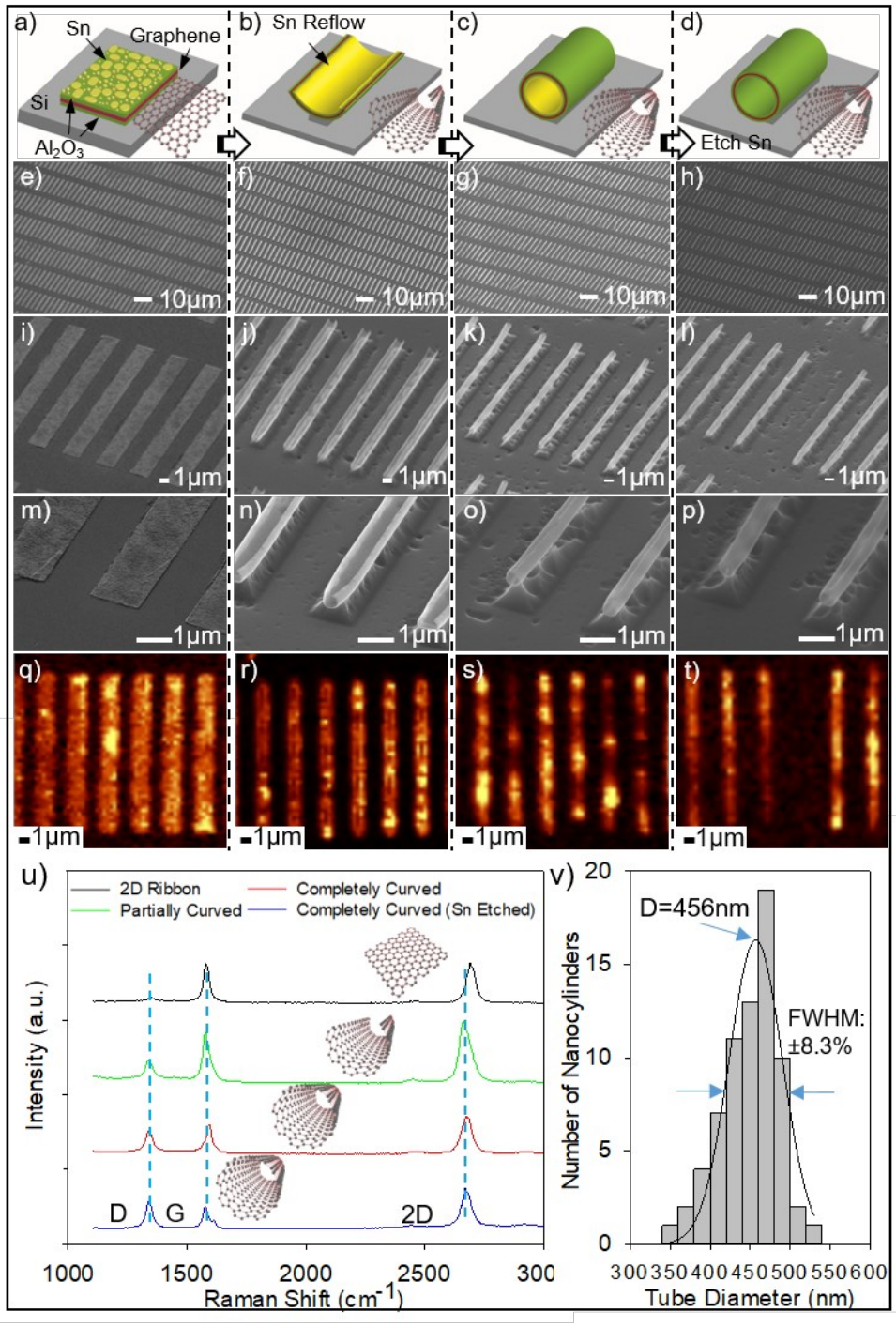

Figure 2. a-d) Conceptual schematics, e-p) SEM images, and q-u) Raman analysis of graphene-based ribbon, partially curved nanocylinder, and 3D nanocylinder triggered by reactive ion etching. a) The 2D graphene-based ribbon (Al_2O_3/ Graphene/ Al_2O_3/ Sn) is formed on a Si substrate. b, c) Reactive ion etching is used to release the 2D ribbon while simultaneously generating a surface tension force to curve the structure into b) partially and c) completely curved nanocylinders. d) After self-curving, the Sn layer is removed by nitric acid. The sample is carefully dried out by critical point dryer. e-p), The high yield of the self-curving process enables the assembly of an array (30 × 100) of nanocylinders, showing the ability to achieve large scale fabrication. q-t) The property of graphene is characterized by Raman imaging based on G band (1590 cm^{-1}) of q) the 2D graphene ribbon, r) partially curved cylinder, s) completely curved cylinder, t) completely curved cylinder after etching showing the same shape as the SEM image (i-l). q) Raman spectrum shows that the two dominant peaks of graphene, G band (~1590 cm^{-1}), and 2D band (~2680 cm^{-1}), are preserved during self-curving, confirming the quality of the intrinsic graphene properties. v) Analysis of uniformity in cylinder diameters between different cylindrical structures on the same sample, the data is based on sampling the diameter for 70 nanocylinders.

A key metric here is preservation of graphene properties during self-assembly by the sandwich layers as revealed by the Raman spectra with dominant G band (~1580 cm^{-1}) and 2D band (~2690 cm^{-1}) [30] and corresponding geometrical transformations observed in mapped Raman images (Figure 2q-u). The nanocylinder arrays possess a relatively high uniformity as evident from the Gaussian curve, defining a full-width half-maximum (FWHM) deviation of only 16.6% in the diameter (Figure 2v). The detailed fabrication process, full Raman details and evaluation, and the measurement of cylinder diameters are described in the Methods section and Supporting Information Figure S1.

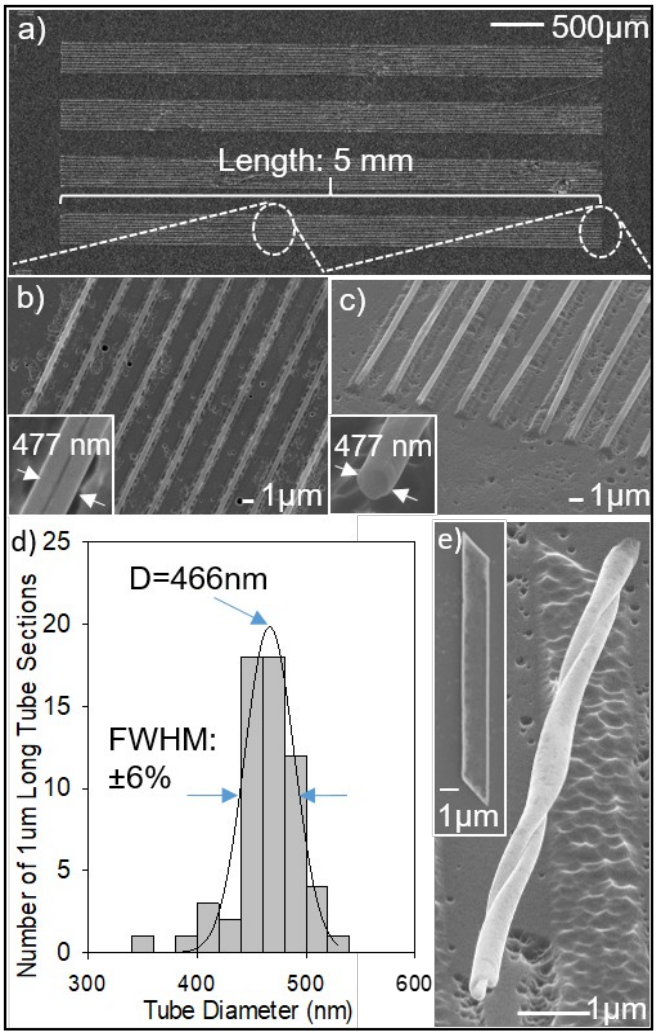

Figure 3. Self-assembly of graphene-based a-d) long and d) twisted nanocylinders. a) SEM image of the overview of the 5 mm long graphene-based nanocylinders with a diameter of 500 nm. b, c) SEM images showing the zoomed-in image of the middle and end of the long nanocylinder, demonstrating uniform self-assembly throughout the structure. d) Analysis of the uniformity of the 5 mm long nanocylinders showing a diameter (D) of 466 nm along the length of cylinder and a FWHM of 6%. e) SEM image of the graphene-based twisted nanocylinder before and after self-assembly. The narrow ends of the ribbon will be released prior to the release of the rest of the structure, folding first. Upon further etching, the folding trend is preserved to achieve the twisted structure.

The shape of the self-assembled graphene-based nanostructure is further controlled via tuning the design of the 2D graphene structures before self-assembly. By patterning the 2D

graphene ribbon with dimensions of 1.5μm×5 mm, graphene-based nanocylinders with a diameter of 477 nm and a high aspect ratio (ratio of the length to the diameter) of around 10,000 are achieved (Figure 3a-c). Even though the length of the self-assembled nanocylinders is in millimeter scale, the two edges closely touch each other throughout the entire length of the structure (Figure 3b,c), forming a uniform nanocylinder. To quantify the uniformity of the 5 mm long graphene nanocylinders, a single tube is divided into multiple sections of 1 μm length. A histogram of the diameter variation in the long nanocylinder (Figure 3d) has an extremely low FWHM of 12%, which can be attributed to the well-defined width of the 2D ribbon and the self-stopping mechanism induced by the touching of two edges. Moreover, this self-curving process is feasible for fabricating 3D graphene nanocylinders with ~~various other~~controlled dimensions. Excluding the limitations ~~of~~ due to the size of graphene sheets and the ~~abilities~~ resolution of the electron beam lithography (EBL) ~~process~~, there is no limit to the length of the 3D graphene nanocylinders. By increasing the length of the 2D design, 3D graphene nanocylinders with significantly higher aspect ratios can be further achieved. Furthermore, instead of previously realized techniques that utilize a mismatch ~~of~~ in crystallographic direction[s] [31], a new strategy for fabricating twisted graphene-based nanocylinders is demonstrated for the reflow induced self-curving process, which is designing 2D ribbons with beveled edges (Figure 3e inset). As the etching rate is isotropic along the outline of the 2D ribbons, the sharp corner is released and starts folding earlier. Thus, a diagonal folding trend ~~is initiated~~propagates from the sharp corner, which determines the folding direction of the whole structure. With further etching, the remainder of the graphene-based ribbon is released and folds up along the initial folding direction, resulting in a twisted graphene-based nanocylinder (Figure 3e). The asymmetrical twisted graphene cylinders are particularly attractive for chiral plasmonic optofluidic sensors that

can provide more detailed information about chiral biological molecules such as proteins and amino acids than conventional achiral spectroscopy-based sensing techniques using planar graphene [32].

The addition of an extra spatial degree of freedom to the 2D plasmonic graphene ribbons, drastically changes the localized surface plasmon resonances (LSPRs) in these structures, and consequently affects the associated near-field enhancement. ~~Comsol~~ COMSOL Multiphysics was used to model the near-field enhancement of the 2D and 3D graphene structures (see details of the simulations in the Methods section). The frequencies of the LSPRs were determined from the transmission spectra of graphene structures (see Supporting Information Figure S2a and Figure S3), and the resulting field enhancements at the resonant frequency were analyzed (Figure 4 and S2). As already shown in Figure 1d-f, the strong field enhancement at the edges of the 2D ribbon, is significantly modified in the case of curved 3D structures due to the increased field coupling between the opposite edges of the structures. Based on the polarization of incident E-field, the coupling in 2D ribbons exists only across the lateral edges (width) of the nanoribbon as an in-plane mode (Figure 4a) due to the large distance between the opposing corners of the ribbon, the field at the two corners cannot directly interact. In contrast, curved 3D structures induce hybridized in-plane edge and out-of-plane radial coupled 3D plasmon modes. As the curvature is increased to form partially curved cylinders, an additional coupling exists between opposing surfaces from the bottom of the cylinder to the two corners due to the decreased gap between them (Figure 4b,c). Finally, at maximum curvature, two forms of field couplings are induced in 3D graphene cylinders (Figure 4d). Firstly, similar to 2D ribbons the plasmons along the entire circular edge (circumference) couple to neighboring points along the edge, forming an in-plane edge mode. Secondly, with the closing of the ribbon

into cylinder geometry, the incident electric field couples more effectively into the azimuthally symmetric cylindrical modes, with the plasmon field extending in the radial out-of-plane direction. ~~Secondly, the small diameter of the cylinder allows the plasmon-generated field to couple across the opening to those points lying radially, horizontally, and vertically across the circumference, forming an out-of-plane radial mode.~~ The simultaneous couplings into these edge and cylindrical modes lead to strong volumetric plasmonic field within the curved graphene ~~The simultaneous edge and radial coupling along the entire circumference form a uniformly coupled mesh across the opening and causes the uniform cross-sectional field at the openings of the cylinder~~ (Figure 1f). The effect of plasmon hybridization in 3D graphene nanocylinders is further accentuated when substrate effects are taken into account. Simulations were carried out for 2D and 3D graphene structures in vacuum (refractive index = 1) and a silicon (Si)-like 1.5 μm thick substrate (refractive index = 3.48). A strong degradation and localization of the plasmon near-field enhancement occurs due to the presence of the substrate, limiting the enhanced field to ~~the corners of the ribbon only~~a smaller spatial area (Figure 4e,i), as opposed to 2D graphene in the vacuum where a uniformly decaying field can be seen across the surface of the ribbon (Figure S2b). When 2D ribbons are curved, the spatial overlap of graphene with the underlying substrates decreases, leading to a corresponding decrease in the substrate influence on the field enhancement. As a result, the partially (50% curved shown in Figure 4f,j and 99% curved shown in Figure 4g,k) and completely curved nanocylinder (Figure 4h,l) structures retain a stronger near-field enhancement spreading over a larger area, similar to freestanding graphene structures in vacuum (Supporting Information Figure S2c,d,e). For a 2D ribbon on a Si substrate, the field enhancement at the edges (~3×10^2) is two orders of magnitude lower than the enhancement for a graphene ribbon in vacuum (Supporting Information Figure S2f,g), which further decays by an

order of magnitude when moving to the center of the ribbon (Figure 4m blue line, with normalized position taken across the ribbon width as shown in Figure 4i). On the other hand, for the halfway curved nanocylinder, a line-type substrate contact (Figure 4f,j) leads to minimal spatial overlap, as opposed to 100% surface-area contact in 2D ribbons. The lower overlap with the substrate, stronger field coupling between the points on the circumference of the cylinder as well as radial field coupling across the nanoscale openings of the cylinder leads to an enhancement (~5.5×10^3) that is two orders of magnitude stronger than in the 2D ribbon and remains constant across the width of the partially curved nanocylinder (Figure 4m green line, with normalized position taken along the semi-circular circumference as shown in Figure 4j). Similarly, the completely curved nanocylinder (Figure 4h) undergoes an even stronger (~2.3×10^4) enhancement, which is nearly two orders of magnitude stronger than for a nanocylinder in vacuum (Figure S2f,g), through additional localized enhancement occurring between the curved graphene and substrate alongside full radial coupling along the circumference at the opening of the nanocylinder. The simultaneous localization and radial couplings give rise to a virtual cross-sectional area of strong field enhancement at the opening of the completely curved nanocylinder (Figure 4l). The 3D plasmon couplings at the openings of the completely curved nanocylinders induce a total integrated edge enhancement of 1149, which is 13 times higher than the total field enhancement of 87 at the edge of the 2D ribbon.

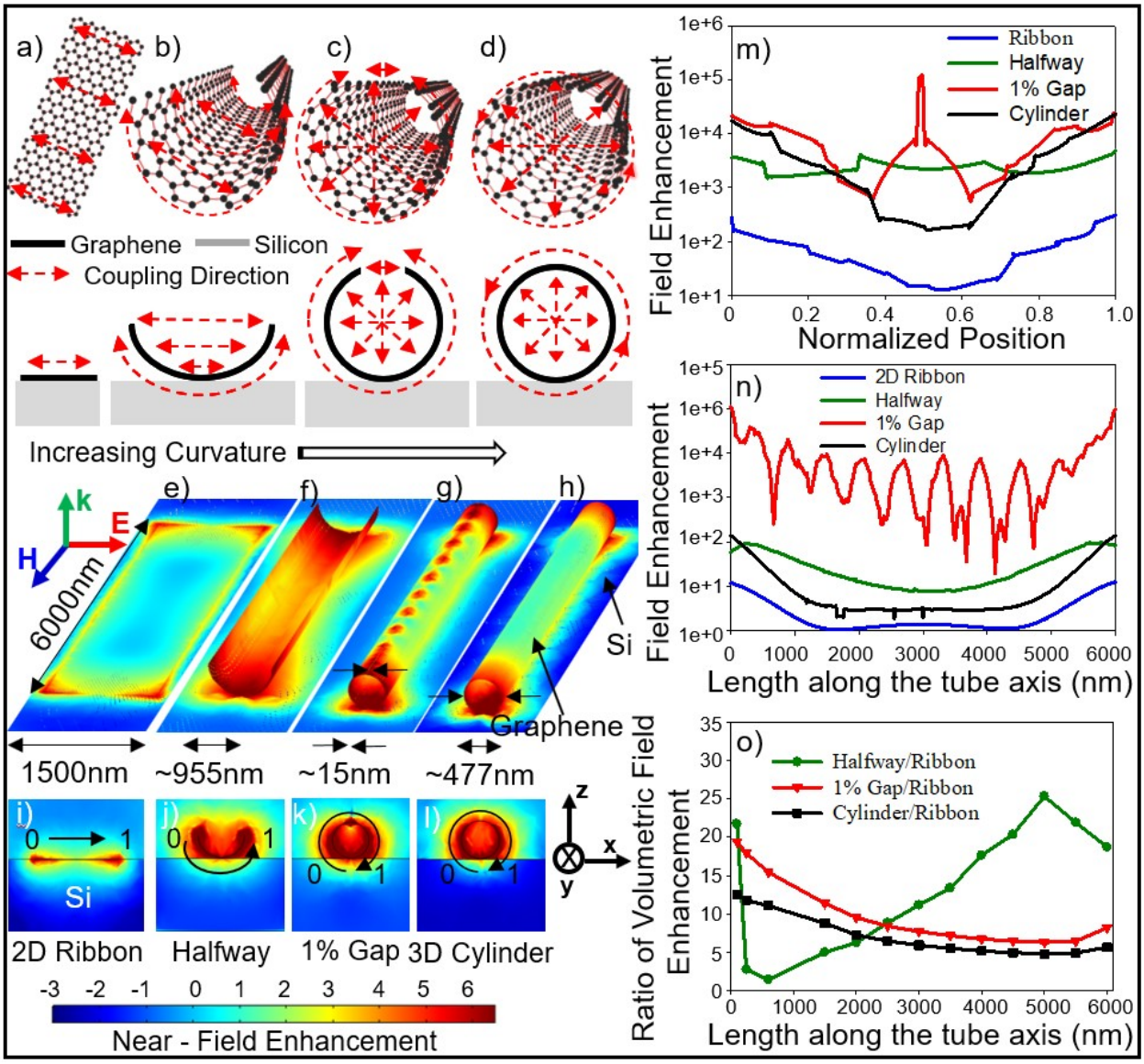

Figure 4. Schematics, and simulation results of the field enhancement in the graphene-based 2D ribbon, half-way curved cylinder, 1% gap cylinder, and completely curved nanocylinder at the frequencies of their geometric resonance as shown in Supporting Information Figure S3. (a-d) 3D and cross-sectional schematics illustrating the coupling directions in 2D ribbons and 3D partially and completely curved cylinders. (e-h) The near-field enhancement plotted on the surface of a a) 2D ribbon, b, c) partially curved cylinders, and d) completely curved cylinders. i-l) The cross-section images show the field enhancement in the ZX plane when an imaginary cut plane is placed at the edge of the structures at 6000 nm. m) The field enhancement in ZX plane along the circumference at the ends of the structures (see the black arrow in i-l)). n) The field enhancements at the center of the gap in the halfway and 1% gap curved cylinders, at the surface of the completely curved cylinder along an imaginary edge, and on the surface of the ribbon. The corresponding values of field enhancement are plotted for the entire length of the structure along structural edges overlapping with cut plane as shown by the black arrow in Supporting Information Figure S5e-h. A strong propagating mode is seen along the edge of the cylindrical structure with 1% gap. o) The volumetric field enhancements along the length of the 3D structures are analyzed based on their ratio to the volumetric field in a 2D graphene ribbon. Volumetric enhancement is calculated by volume integrals of the field

inside the 3D structures and for an imaginary rectangular box of thickness 119 nm placed on the 2D ribbon with lengths increasing from 100 nm to 6 μm. For all the cases m-o), the 3D cylindrical structures show stronger field enhancement compared to the 2D ribbon. The primary geometric resonant frequencies for the ribbon, halfway, 1% gap, and completely curved nanocylinders in e-o were found to be 3.6, 7.7, 14.3, and 12.6 THz, respectively.

Moreover, the field enhancement induced in the 3D nanocylinder can be further boosted via controlling the gap in the nanocylinder. As shown in Figure 3b,c even for the completely curved nanocylinder structures, a sub-10 nm gap exists between the two curved edges joining together which introduces edge effects along the length of the structure. Simulations for the 99% curved nanocylinders (Figure 4g,k) reveal strong interactions between the two edges separated by a distance of only 15 nm that further enhances the coupled field at the center of the gap by an order of magnitude (Figure 4m, red line). It should be noted that inside the 15 nm gap of the 99% curved nanocylinder, the field enhancement is 300 times stronger than the maximum enhancement obtained even at the edge of the 2D ribbons (Figure 4m). The geometrically confined field in the partially curved nanocylinders exists along the entire length of the nanocylinders (Figure 4g, Figure S5c). This leads to a field enhancement 4 orders of magnitude (Figure 4n, red line) stronger when compared to that at the center of the 2D ribbon (Figure 4n, blue line). Oscillations in the field strength (Figure 4n, red line), indicate the highly confined propagating mode within the plasmonic gap in a 99% curved nanocylinder with a 15 nm gap. The strongly confined, high-enhancement, propagating edge modes are particularly attractive for the development of graphene-based optoelectronic devices including plasmonic waveguides to achieve exceptional propagation lengths and figure of merit [33-35]. The completely curved nanocylinder does not show propagating edge modes along the length of the cylinder, thus, supporting the conclusion that these modes in the nearly curved (1% gap) nanocylinders are purely longitudinal edge modes. However, even in the absence of the longitudinal edge modes

(at the center of the completely curved nanocylinders), the 3D radially curved coupling boosts that field enhancement by an order of magnitude compared to the center of 2D ribbons (Figure S4). The strong uniform field enhancement at the openings of the nanocylinders induced by hybridized radial and edge couplings (Figure 4j-l) can also be termed as volumetric enhancement, which is computed as an integral of the field enhancement at the cross-section of the openings. The total volumetric enhancement for the uniform field in a halfway curved nanocylinder is 20 times higher than the volumetric field in 2D ribbons over the full length (6 μm) of the structures (Figure 4o, green line and Figure S6). To theorize the plasmonic properties in the fabricated low-defect regime nanocylinders (Figure 2), the impact of defect concentration (computed as ratio of D-band to G-band intensities, I_D/I_G) on the relaxation time and near-field enhancement was also obtained (details in Supporting Information). Even with a reduced relaxation time that is an order of magnitude lower than that in 2D ribbons, the 3D cylinders demonstrate a volumetric enhancement that is 4 times stronger than the volumetric enhancement obtained for 2D ribbons.

The near-field enhancement as a result of edge-substrate interactions and radial coupling stemming from the curvature (Figure 4) can be a key parameter in the development of higher sensitivity biological sensors. The virtual cross-sectional area of strong uniform field at the opening of the 3D nanocylinders (Figure 4h,i) can be leveraged for the fabrication of cylindrical vein-like plasmonic optofluidic channels for analysis of molecules flowing within them. Since every molecule traversing through the 3D channel must pass through the virtual cross-sectional area at the opening of the nanocylinder, the strongly enhanced field interacts with each of the molecules, thereby preventing limitations in sensitivity arising from the need for the molecules to diffuse to the graphene ribbon surface as is the case in 2D graphene sensors. Simulations for the

sensing-based advantages of the plasmon modes in cylinders reveal that any specimens that are inside the cylinder even at the center (maximum distance from graphene surface) experience an induced field that is almost 2 orders of magnitude stronger than in 2D ribbons. Moreover, a resonant frequency shift that is 75 times stronger than 2D ribbon is induced by even a 2 nm layer of the targeted analyte for the 3D cylinders. A detailed discussion of the sensing behavior of 3D graphene structures tubes has been included elsewhere. (Agarwal, K.; Cho, J. H. Plasmonic Optofluidic Sensing in Self-assembled 3D Graphene Geometries. Submitted for publication)

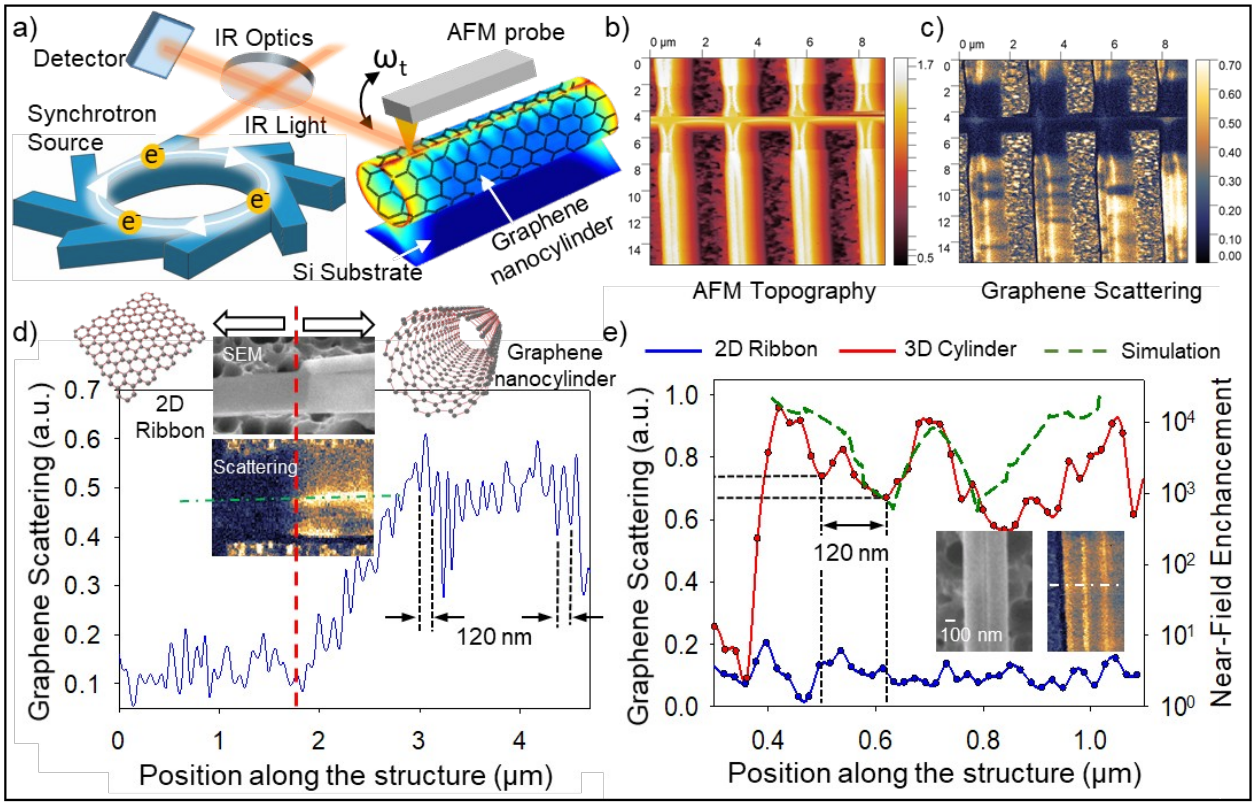

Figure 5. a) Schematic illustration of the measurement setup for SINS analysis of 3D graphene where IR radiation from a synchrotron beamline is used in an s-SNOM measurement. b) AFM topology images plotted with color bar in micrometer scale, showing two distinct regions of 2D and 3D regions on the substrate. c) SINS broadband IR image captured for the same topography area as shown in (b) obtained through mapping of the second harmonic optical amplitude signal with distinct change between the 2D and 3D graphene regions. The scale bar shows the amplitude in volts. d) Scattering data extracted along the longitudinal direction from the scattering images showing the low scattering in 2D regions and the strong plasmon-driven resonant scattering in 3D cylinder regions (inset: a SEM image and a corresponding scattering image of the sample, data were extracted along the green line). e) Graph showing the collected scattering data across the width of the cylinders, 2D ribbons, and simulations with data for cylinders

acquired from position as marker by white line in the inset, the dashed lines mark the plasmon wavelength. The sinusoidal variation of the scattering corresponds to the plasmon interference fringes.

The SINS technique was used to measure and experimentally visualize the plasmon-induced near-field enhancement in graphene nanocylinders (Figure 5a,) because of unique advantages from the AFM-tip (atomic force microscopy) enhanced probing of the coupled edge plasmons and ~~the non-Reststrahlen limited optics with~~ spectral range, high spectral brightness, and coherence of the source [36-39]. The SINS data reveals an overlap between graphene nanocylinder topography (Figure 5b) and IR scattering images (Figure 5c) to validate optical properties of graphene. The scattering images reveal hybridized plasmons being launched along the surface of the graphene cylinders and being reflected by the edge. Quantitative analysis of the scattering data demonstrates a marked transition with increase from ~0.1V in 2D graphene to ~0.6V in the 3D cylindrical graphene domains (Figure 5d), thus, demonstrating the lower losses in the graphene plasmons stemming from their curvature. The interaction of the small gap longitudinal edges within the curved graphene cylinders gives rise to high-intensity hybridized edge-based near-field enhancement mode revealed by the stronger scattering along the edges in the scattering images (Figure ~~5e~~5d) and in the data extracted from these images similar to simulated near-field enhancement (Figure ~~5d~~5e). On the other hand, the losses and the lower spatial coverage of the near-field in the 2D ribbons correspond to nearly no scattering signals recorded over them (Figure ~~5d~~5e, blue line). A detailed analysis of the line scan image profiles (Figure ~~5e~~5d,~~de~~) reveals a plasmon wavelength of ~~120~~ 240 nm (twice the distance between successive fringes). ~~The corresponding incident wavelength that induces plasmon resonance was found using third harmonic generation, which shows a clear peak at a wavenumber of 666.74 cm^{-1} i.e. a wavelength of 15 μm (Figure 5f, blue line). The incident wavelength information from the~~

~~peak is further complemented by the change in phase slope also seen in the acquired spectra for the same wavenumber (Figure 5f, red line). This implies a confinement factor of 125 i.e. more than 2 orders of magnitude (details in Supporting Information).~~ The result can be directly compared to the simulated data for the structures, which show a similar four order of magnitude near-field increase on the graphene cylinder ~~(Figure 5e, green line)~~ for a resonant absorption peak at 20 μm (14.3 THz). It should be noted that the SINS measurement data ~~from~~ for the nanocylinders provides the first evidence of hybridized plasmonics ~~absorption~~ in well-defined 3D graphene geometries on a Si substrate where the data shows i) superior ~~absorption~~ plasmon resonances in 3D graphene compared to 2D graphene, ii) a confinement of ~~two~~ four orders of magnitude, and iii) ~~lower susceptibility to substrate induced losses in nanocylinders~~higher compatibility of plasmon resonance graphene cylinders.

Conclusion

In conclusion, this work introduces 3D plasmon modes, hybridized edge (in-plane) and radial (out-of-plane) coupled plasmons, generated in self-assembled graphene-based cylindrical nanostructures. The radial coupling of plasmons lead to a uniform circular cross-sectional area of extreme near-field enhancement at the openings of the 3D nanocylinders. The hybridized edge couplings in the curved graphene nanocylinders induce a propagating edge mode throughout the length of the cylinders with an electric field that is 4 orders of magnitude stronger than in the 2D ribbons. SINS-based scattering~~absorption~~ images visualized the hybridized 3D plasmon modes and verified a confinement factor of ~~over 2~~4 orders magnitude in the 3D graphene nanocylinders. The unique spatial coupling within 3D structures extends the near-field enhancement into the bulk cross-sectional 3D space allowing the architecture to be

utilized for the realization of cylindrical plasmonic channels.

Methods

Fabrication of three-dimensional graphene nanocylinders:

3D graphene nanocylinders are realized via plasma triggered self-assembly of 2D graphene-based ribbons [3 nm thick aluminum oxide (Al_2O_3)/single layer graphene/3 nm thick Al_2O_3/5nm tin (Sn)] which is defined on high resistivity Si substrate by standard EBL and graphene wet transfer process. After self-assembly, the Sn layer in 3D graphene nanocylinders is removed by nitric acid. Then, the nanocylinder sample– is transferred into IPA (isopropyl alcohol) and is gently dried out in a critical point dryer to minimize the effect of capillary force Raman spectroscopy and imaging are carried out to investigate the changes of graphene properties. A detailed description of these processes is given in the Supporting Information.

Analysis of nanocylinder uniformity:

The uniformity of different nanocylinders within the array (Figure 2h) is evaluated based on a previously developed method [40]. The diameter of seventy nanocylinders is measured and be plotted into a histogram (Figure. 2v). After applying Gaussian curve fitting, the full-width at half-maximum (FWHM) is used as the data to evaluate uniformity. Based on the measurement, FWHM is 16.6% for the array of the nanocylinders, which shows relative high uniformity. To quantify the uniformity of the 5 mm long graphene nanocylinders, a single tube is divided into sixty sections of 1 μm length, such that a histogram of their diameter (Figure 3d) has FWHM of this long nanocylinder is 12%, which is 6% lower than the previous work [40].

Simulation setup for two- and three-dimensional graphene structures:

2D and 3D Graphene structures were simulated using Comsol Multiphysics version 5.2a with the conductivity of graphene as given by the Kubo Formula for 0.4 eV Fermi level [41]. Simulation setup and parameters are discussed in detail in the Supporting Information.

SINS Measurements: ~~setup for three-dimensional graphene structures:~~

To measure and experimentally visualize the plasmon-induced near-field enhancement in graphene nanostructures, the samples were chemically doped with nitric acid vapor for 5 minutes to induce p-type doping with increased hole concentration and open a bandgap in graphene. SINS measurements were performed using synchrotron infrared radiation from Beamline 2.4 at the Advanced Light Source in combination with a commercial s-SNOM instrument (neaSNOM, neaspec GmbH) and a modified Ge:Cu detector (REF 39). The instrument consists of an asymmetric Michelson interferometer, in which incident light is split by a beamsplitter (KRS-5) and directed to either a flat, moving mirror or focused onto an AFM tip scanning in close proximity to the sample. The backscattered light from the AFM tip is recombined on the beamsplitter with light from flat mirror and focused onto the IR detector. The resulting interference signal is demodulated at harmonics of the tip-tapping frequency and Fourier-transformed to yield near-field infrared amplitude and phase spectra. "White-light" broadband IR images are measured by holding the moving mirror fixed at the zero path difference (ZPD) position and acquiring the demodulated amplitude signal while scanning the AFM. For these measurements, the incident light is polarized primarily orthogonal to the sample surface, but focus angle includes an in-plane component that was ~~The 3D graphene cylinder samples were tilted at an angle of 45 degree to the surface and the incident light~~ polarized along the width of the ribbon (See Supporting Information for more details). ~~The SINS technique allows line scans~~

~~in AFM tapping mode along the top edge of the graphene cylinders as shown in Figure 5a. The 3D graphene cylinder samples were tilted at an angle of 45 degree to the surface and the incident light polarized along the width of the ribbon (See Supporting Information for more details). The mapped images of the second harmonic deflection provide a visualization of the absorption in 3D graphene. Line scans profile images have sinusoidally varying absorption that cause voltage maxima and minima on the graphene corresponding to the plasmon interference fringes. The distance between successive minima or maxima can be measured to directly acquire the plasmon wavelength as shown in Figure 5c.~~

Acknowledgement

This research was supported by the National Science Foundation under Grant No. CMMI-1454293. The authors also acknowledge the Minnesota Supercomputing Institute (MSI) at the University of Minnesota for providing computing resources that contributed to the simulation results reported within this paper. Portions of this work were conducted in the Minnesota Nano Center, which is supported by the National Science Foundation through the National Nano Coordinated Infrastructure Network (NNCI) under Award Number ECCS-1542202. Parts of this work were carried out in the Characterization Facility, University of Minnesota, a member of the NSF-funded Materials Research Facilities Network (www.mrfn.org) via the MRSEC program. This work was also supported partially by the National Science Foundation through the University of Minnesota MRSEC under Award Number DMR-1420013. This research used resources of the Advanced Light Source, a U.S. DOE Office of Science User Facility under contract no. DE-AC02-05CH11231.

Author Information

Chunhui Dai and Kriti Agarwal contributed equally to this work.

Affiliations

Department of Electrical and Computer Engineering, University of Minnesota, Minneapolis, MN, 55455, USA

Chunhui Dai, Kriti Agarwal, Chao Liu, Daeha Joung, Andrei Nemilentsau, Qun Su, Tony Low, Steven Koester, and Jeong-Hyun Cho

Advanced Light Source Division, Lawrence Berkeley National Laboratory, Berkeley, California, 94720, USA

Hans Bechtel

Author contributions

C. Dai and K. Agarwal contributed equally to this work. J. H. C. conceived the idea and supervised this work. C. D., C. L., D. J., and J. H. C. developed the fabrication process for the 3D cylinders and performed the Raman analysis. K. A. and J. H. C. conducted the Comsol simulations of the 2D and 3D graphene structures. D. J. and C.L. assisted in the fabrication and data analysis. A. N. and T. L. assisted in the simulation setup for 3D graphene. Q. S. and S. K. assisted the 2D graphene growth. H. B. conducted the SINS measurement for the graphene J. H. C., C. D., and K. A. jointly wrote the manuscript.

Reference

1. Tokura, Y. et al. Polymer tube nanoreactors via DNA-origami templated synthesis. Chem Commun **54**, 2808-2811(2018)
2. Childres, I., Jauregui, L. A., Park, W., Cao, H. & Chen, Y. P. Raman spectroscopy of graphene and related materials. New Developments in Photon and Materials Research (2013).
3. Cancado, L. Quantifying Defects in Graphene via Raman Spectroscopy at Different Excitation Energies. Nano Lett. **11**, 3190-3196(2011).
4. Wong, J. H., Wu, B. R., and Lin, M. F. Strain Effect on the Electronic Properties of Single Layer and Bilayer Graphene. J. Phys. Chem. C **116**, 8271-8277(2012)
5. Choi, S. M., Jhi, S. H., and Son, Y. W. Effects of strain on electronic properties of graphene. Phys. Rev. B **81**, 081407 (2010)
6. Koppens, F. H., Chang, D. E. & Garcia de Abajo, F Javier. Graphene plasmonics: a platform for strong light–matter interactions. Nano Lett. **11**, 3370-3377 (2011).
7. Liu, F. & Cubukcu, E. Tunable omnidirectional strong light-matter interactions mediated by graphene surface plasmons. Phys. Rev. B **88**, 115439 (2013).
8. Xu, W., Mao, N. & Zhang, J. Graphene: a platform for surface-enhanced Raman spectroscopy. Small **9**, 1206-1224 (2013).
9. Yang, X. et al. Nanomaterial-Based Plasmon-Enhanced Infrared Spectroscopy. Adv. Mater. **30**, 1704896 (2018).
10. Low, T. & Avouris, P. Graphene plasmonics for terahertz to mid-infrared applications. ACS Nano **8**, 1086-1101 (2014).

11. Li, Y. et al. Graphene plasmon enhanced vibrational sensing of surface-adsorbed layers. Nano Lett. **14**, 1573-1577 (2014).

12. Fei, Z., M. D. Goldflam, J-S. Wu, S. Dai, M. Wagner, A. S. McLeod, M. K. Liu et al. "Edge and surface plasmons in graphene nanoribbons." Nano letters 15, no. 12 (2015): 8271-8276.

13. Freitag, M., Low, T., and Avouris, P. "Increased responsivity of suspended graphene photodetectors." Nano letters 13, no. 4 (2013): 1644-1648.~~Increased responsivity of suspended graphene photodetectors~~

14. Yan, H., Low, T., Zhu, W. et al. "Damping pathways of mid-infrared plasmons in graphene nanostructures." Nature Photonics 7, 394–399 (2013).~~Multilayer friction and attachment effects on energy dissipation in graphene nanoresonators~~

15. Yan, H., Li, X., Chandra, B., Tulevski, G., Wu, Y., Freitag, M., Zhu, W., Avouris, P. and Xia, F., 2012. Tunable infrared plasmonic devices using graphene/insulator stacks. Nature nanotechnology, 7(5), pp.330-334.

16. Rodrigo, D., Tittl, A., Limaj, O., De Abajo, F.J.G., Pruneri, V. and Altug, H., 2017. Double-layer graphene for enhanced tunable infrared plasmonics. Light: Science & Applications, 6(6), pp.e16277-e16277.

17. Gomez-Diaz, J.S., Moldovan, C., Capdevila, S., Romeu, J., Bernard, L.S., Magrez, A., Ionescu, A.M. and Perruisseau-Carrier, J., 2015. Self-biased reconfigurable graphene stacks for terahertz plasmonics. Nature communications, 6(1), pp.1-8.

18. Zhu, W., Low, T., Perebeinos, V., Bol, A.A., Zhu, Y., Yan, H., Tersoff, J. and Avouris, P., 2012. Structure and electronic transport in graphene wrinkles. Nano letters, 12(7),

pp.3431-3436.~~Chen, R., Yang, C., Jia, Y., Guo, L. and Chen, J., 2019. Plasmon reflection reveals local electronic properties of natural graphene wrinkles. Chinese Physics B, 28(11), p.117302.~~

19. Yang, C., Chen, R., Jia, Y., Guo, L. and Chen, J., 2017. Asymmetrical plasmon reflections in tapered graphene ribbons with wrinkle edges. Chinese Physics B, 26(7), p.074220.
20. Slipchenko, T.M., Nesterov, M.L., Hillenbrand, R., Nikitin, A.Y. and Martín-Moreno, L., 2017. Graphene plasmon reflection by corrugations. ACS Photonics, 4(12), pp.3081-3088.
21. Fei, Z., Foley IV, J.J., Gannett, W., Liu, M.K., Dai, S., Ni, G.X., Zettl, A., Fogler, M.M., Wiederrecht, G.P., Gray, S.K. and Basov, D.N., 2016. Ultraconfined plasmonic hotspots inside graphene nanobubbles. Nano letters, 16(12), pp.7842-7848.
22. Yue, K., Gao, W., Huang, R. and Liechti, K.M., 2012. Analytical methods for the mechanics of graphene bubbles. Journal of Applied Physics, 112(8), p.083512.
23. ~~58.~~ Blees, M.K., Barnard, A.W., Rose, P.A., Roberts, S.P., McGill, K.L., Huang, P.Y., Ruyack, A.R., Kevek, J.W., Kobrin, B., Muller, D.A. and McEuen, P.L., 2015. Graphene kirigami. Nature, 524(7564), pp.204-207.
24. ~~59.~~ Miskin, M.Z., Dorsey, K.J., Bircan, B., Han, Y., Muller, D.A., McEuen, P.L. and Cohen, I., 2018. Graphene-based bimorphs for micron-sized, autonomous origami machines. Proceedings of the National Academy of Sciences, 115(3), pp.466-470.
25. ~~60.~~ Costa, A.T., Ferreira, M.S., Hallam, T., Duesberg, G.S. and Neto, A.C., 2013. Origami-based spintronics in graphene. EPL (Europhysics Letters), 104(4), p.47001.

26. ~~61.~~ Xu, W., Qin, Z., Chen, C.T., Kwag, H.R., Ma, Q., Sarkar, A., Buehler, M.J. and Gracias, D.H., 2017. Ultrathin thermoresponsive self-folding 3D graphene. Science advances, 3(10), p.e1701084.

27. ~~62.~~ Joung, D., Nemilentsau, A., Agarwal, K., Dai, C., Liu, C., Su, Q., Li, J., Low, T., Koester, S.J. and Cho, J.H., 2017. Self-assembled three-dimensional graphene-based polyhedrons inducing volumetric light confinement. Nano letters, 17(3), pp.1987-1994.

28. ~~63.~~ Agarwal, K., Dai, C., Joung, D. and Cho, J.H., 2018. Nano-Architecture Driven Plasmonic Field Enhancement in 3D Graphene Structures. ACS nano, 13(2), pp.1050-1059.

29. ~~Curving Nanostructures Using Extrinsic Stres~~ Cho, J.H., James, T. and Gracias, D.H., 2010. Curving nanostructures using extrinsic stress. Advanced Materials, 22(21), pp.2320-2324.~~s~~

30. Childres, I., Jauregui, L. A., Park, W., Cao, H. & Chen, Y. P. Raman spectroscopy of graphene and related materials. New Developments in Photon and Materials Research (2013).

31. Schmidt, O. G., Schmrje, N., Deneke, C., Muller, C., Jin-Phillipp, N. Y. Three-Dimensional Nano-Objects Evolving from a Two-Dimensional Layer Technology, Adv. Mater. 13, 756-759 (2001)

32. Hentschel, M., Schäferling, M., Duan, X., Giessen, H. & Liu, N. Chiral plasmonics. Sci. Adv. 3, e1602735 (2017).

33. Zhang, B. et al. Hybrid dielectric-loaded nanoridge plasmonic waveguide for low-loss light transmission at the subwavelength scale. Sci. Rep. 7, 40479 (2017).

34. Fang, Y. & Sun, M. Nanoplasmonic waveguides: towards applications in integrated

nanophotonic circuits. Light Sci. App. 4, e294 (2015).

35. Berini, P. Figures of merit for surface plasmon waveguides. Opt. Express 14, 13030-13042 (2006).
36. Razeghi, M., Lu, Q.Y., Bandyopadhyay, N., Zhou, W., Heydari, D., Bai, Y. and Slivken, S., 2015. Quantum cascade lasers: from tool to product. Optics express, 23(7), pp.8462-8475.
37. Fujita, K., Jung, S., Jiang, Y., Kim, J.H., Nakanishi, A., Ito, A., Hitaka, M., Edamura, T. and Belkin, M.A., 2018. Recent progress in terahertz difference-frequency quantum cascade laser sources. Nanophotonics, 7(11), pp.1795-1817.
38. Barcelos, I.D., Bechtel, H.A., de Matos, C.J., Bahamon, D.A., Kaestner, B., Maia, F.C. and Freitas, R.O., 2019. Probing Polaritons in 2D Materials with Synchrotron Infrared Nanospectroscopy. Advanced Optical Materials, p.1901091.
39. Khatib, O., Bechtel, H.A., Martin, M.C., Raschke, M.B. and Carr, G.L., 2018. Far infrared synchrotron near-field nanoimaging and nanospectroscopy. ACS Photonics, 5(7), pp.2773-2779.
40. Schmidt, O. G., et al. Self-Assembled Nanoholes, Lateral Quantum-Dot Molecules, and Rolled-Up Nanotubes, IEEE J. Sel. Top. Quantum Electron, 8, 1025-1034 (2002)
41. Gusynin, V., Sharapov, S. & Carbotte, J. Magneto-optical conductivity in graphene. J. Phys. Condens. Matter 19, 026222 (2006).58. Hanson, G. W. Dyadic Green's functions and guided surface waves for a surface conductivity model of graphene. J. Appl. Phys. 103, 064302 (2008).
42. Ryu, S., Maultzsch, J., Han, M. Y., Kim, P. & Brus, L. E. Raman spectroscopy of lithographically patterned graphene nanoribbons. ACS Nano 5, 4123-4130 (2011).

43. Ju, L. et al. Graphene plasmonics for tunable terahertz metamaterials. Nature Nanotechnol. 6, 630 (2011).

44. Yan, H. et al. Damping pathways of mid-infrared plasmons in- graphene nanostructures. Nat. Photon. 7, 394 (2013)

45. Ooi, K. et. al. Highly Efficient Midinfrared On-Chip Electrical Generation of Graphene Plasmons by Inelastic Electron Tunneling Excitation. Phys. Rev. Appl. 3, 054001(2015)

46. Jablan, M., Hrvoje B., and Marin S. Plasmonics in graphene at infrared frequencies, Phys. Rev. B 80, 245435(2009)

47. Dai, C. Agarwal, K. and Cho, J. H. Ion-Induced Localized Nanoscale Polymer Reflow for Three-Dimensional Self-Assembly. ACS nano 12, 10251-10261 (2018)

48. Dean, C. R. et al. Boron nitride substrates for high-quality graphene electronics. Nat. Nanotechnol. 5, 722 (2010).

Supporting Information

Hybridized Radial and Edge Coupled 3D Plasmon Modes in Self-Assembled Graphene Nanocylinders

Chunhui Dai[#1], Kriti Agarwal[#1], Hans A. Bechtel[2], Chao Liu[1], Daeha Joung[1], Andrei Nemilentsau[1], Qun Su[1], Tony Low[1], Steven Koester[1], and Jeong-Hyun Cho[1*]

1. Department of Electrical and Computer Engineering, University of Minnesota, Minneapolis, Minnesota 55455, USA
2. Advanced Light Source Division, Lawrence Berkeley National Laboratory, Berkeley, 94720, California, USA

jcho@umn.edu

List of contents

1. Fabrication Process

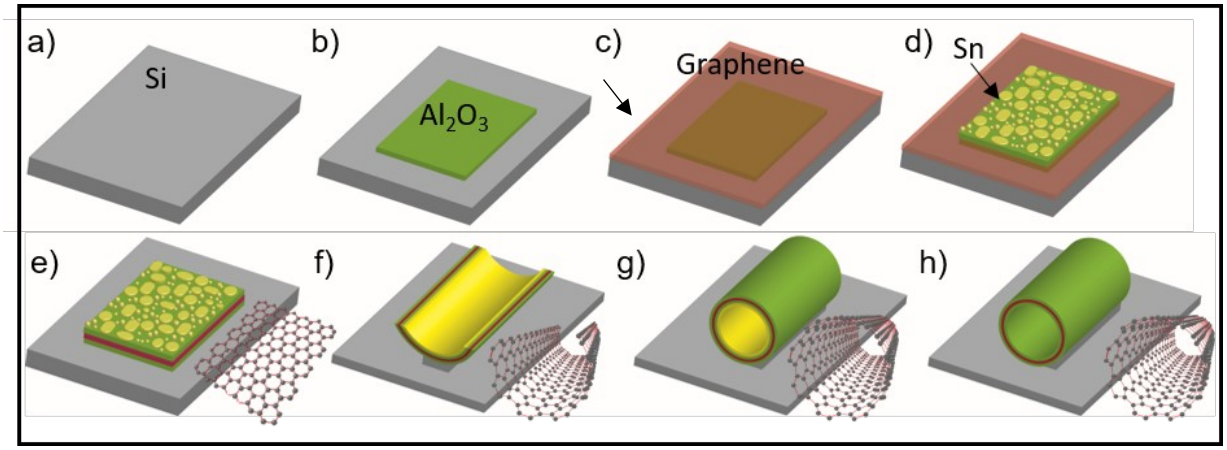

Figure S1. Conceptual schematics of the fabrication process of graphene-based ribbon, half-way folded nanocylinder, and 3D nanocylinder triggered by reactive ion etching. a-d) Schematics showing the fabrication of 2D ribbon contains 3 nm Al_2O_3/monolayer graphene/3 nm Al_2O_3/5nm Sn. e), The undesired Graphene is removed by oxygen plasma etching. f-g) After being treated in a reactive ion etching system, Sn film will melt and experience metal reflow due to the heat generation in etching process, which induce surface tension force to fold the 2D ribbons out of plane to be 3D half-way and completely curved nanocylinder. h) The Sn layer is removed by nitric acid and the nanocylinder is dried out by critical point dryer. The diameter of the nanocylinder is around 500 nm after self-assembly

To fabricate the 3D graphene-based nanocylinders, 2D sandwiched graphene ribbon (3 nm thick Al_2O_3/single layer graphene/3 nm thick Al_2O_3/5 nm thick Sn) was first fabricated (Supporting Information Figure S1a-e). Polymethyl Methacrylate (PMMA) A3 was spun at 3000 RPM on top of the high resistivity Si substrate (560 – 840 Ω·cm) as the electron beam (E-beam) resist. An array of 2D ribbons, with ribbon dimensions of 1.5 μm × 15 μm, was then defined on the PMMA by an EBL system (Vistec EBPG5000+). After developing in MIBK (methyl isobutyl ketone): IPA (isopropyl alcohol) with the ratio of 1:3 for 1 minute, 3 nm thick Al_2O_3 was deposited by an electron beam evaporator (RME-E2000) to form the bottom protection layer (Supporting Information Figure S1b). A lift-off process was carried out in acetone to remove the undesired material. Next, a single layer of chemical vapor deposited (CVD) graphene was transferred on top of the patterned Al_2O_3 ribbon through a wet transfer process (Supporting Information Figure S1c). The mobility of the CVD graphene grown on the copper (Cu) foil is around 2700 $cm^2/V{\cdot}s$. After graphene transfer, N2403 was spun on top of the structure at 5000 RPM as the negative E-beam resist, which can protect graphene from electron irradiation for the rest of the EBL process. Then, a secondary array of 2D ribbons with the same ribbon dimensions (1.5 μm × 15 μm) was defined on the N2403 resist, which was aligned precisely to the bottom protection layer. MF-319 was used as the developer, which dissolved the unexposed resist in 1 minute. Then, 3 nm Al_2O_3 and 5 nm Sn layers were deposited by an electron beam evaporator to form the top protection layer and the sacrificial layer for inducing surface tension force, respectively (Supporting Information Figure S1d). Subsequently, the unwanted graphene areas, which were not protected by Sn and Al_2O_3, were removed by an oxygen plasma treatment in a reactive ion etching (RIE) system (STS 320) (Supporting Information Figure S1e). After fabrication of 2D sandwiched graphene ribbons, RIE with CF_4/O_2 was used to achieve self-

assembly of 3D nanocylinders (Supporting Information Figure S1f,g). During this process, both the chemical reaction between the fluorine atoms and the Si substrate and the physical ion bombardment on the Si substrate can contribute to etching the Si underneath the graphene sandwiched structures (Supporting Information Figure S1f,g). Finally, the graphene sandwiched structures were released from the substrate. Simultaneously, both the physical and chemical reactions generate thermal energy, which melts the Sn, triggering grain coalescence. As a result of grain coalescence, surface tension force was induced in the film, curving the 2D structure out-of-plane to form the 3D nanocylinders (Supporting Information Figure S1g). After self-assembly, the Sn layer could be etched way by immersing into a nitric acid for 30 minutes. To minimize the effect of the capillary force, the sample is transferred into IPA bath and gently dried out in a critical point dryer (CPdryer 915B) (Figure S1h).

2. Raman spectroscopy:

A Witec Alpha300R Confocal Raman Microscope was used for Raman measurement to characterize the graphene quality before and after self-assembly. The system was equipped with a Nikon 100× oil immersion objective for focusing. The laser used in the measurement was a 514.5 nm monochrome argon ion laser with a maximum power of 50 mW. For the detection of the signal, a UHTS300 spectrometer and DV401 CCD detector was used. During the measurement, the samples were mounted on a highly linear, piezo-driven, feedback-controlled scan stage, which can move in x and y directions with a positional accuracy of 5 nm. For the spectral measurement, the laser was carefully focused on the sample (graphene ribbon, partially curved nanocylinder, and completely curved nanocylinder). For the Raman Mapping measurement, the mapping area was setup to be $20 \times 20\ \mu m^2$ with a resolution of 250 nm, which is the optical resolution of the system. The Raman image was generated based on the G band intensity between 1560 cm^{-1} and 1600 cm^{-1}. After measurement, the software, Project FOUR, was used for analyzing data and plotting the spectrum.

In the Raman spectra collected from the 2D graphene ribbons and the partially and completely curved graphene nanocylinders, both dominant peaks of graphene, G and 2D bands, are observed, proving that no critical damage is induced in the graphene (Figure 2u). After self-assembly, the D band (~1350 cm^{-1}) peak, representing defect and lattice disorder, appears and it is stronger for samples with longer self-assembly times (Figure 2u). The higher defect level could be attributed to the increased density of edge defects and lattice disorder caused by stress or wrinkles induced during self-assembly. After self-curving, the edges of the ribbons curve towards the middle of the cylinder and cause a higher density of edge defects and lattice structural stress, leading to higher D band. To further quantify the defect level, the ratio of the D

band intensity (I_D) and G band intensity (I_G), I_D/I_G, is calculated, which is around 1 (representing low defect regime [30]) for completely curved graphene nanocylinders. In addition, the I_D/I_G ratio of about 1 is comparable with a lithographically prepared graphene ribbon [42], which means the properties of graphene are not severely affected by the self-assembly process. Raman images plotted based on G band are collected from samples consisting of entirely 2D graphene ribbons (Figure 2i), partially curved graphene nanocylinders (Figure 2j), and completed curved graphene nanocylinders (Figure 2k) to evaluate the overall graphene status throughout the structures (Figure 2m-o). For the 2D graphene ribbons (Figure 2i), the Raman mapping image shows ribbon structures with the same dimensions of 1.5 μm × 15 μm (Figure 2q), indicating the high quality of the fabricated 2D graphene ribbons. After partially curved, the structures in the Raman image (Figure 2r) have the same reduced width as the curved nanocylinders shown in the corresponding scanning electron microscopy (SEM) image (Figure 2j). When the graphene nanoribbons are completely curved (Figure 2k), a continuous clear Raman image with dimensions of around 477 nm × 15 μm is still observed (Figure 2s), demonstrating the physical properties of graphene are preserved during the self-assembly because of the graphene being sandwiched between two different 3 nm thick layers of Al_2O_3. The ratio of the D-band to G-band intensities in the 3D halfway (0.357) and completely (1.063) curved nanocylinder is in the low-defect regime compared to pristine graphene (0.058). In addition, the effect of Sn etching on the graphene property is characterized by Raman image (Figure 2t) and Raman Spectrum (Figure 2u). The Raman image shows continuous shape that is similar to the nanocylinders after Sn etching (Figure 2l). Though the I_D/I_G ratio is slightly increased to 1.2, it still remains in the low defect regime. Both these two characterization results confirm the high quality of graphene after Sn removal process.

3. Simulation setup for 2D and 3D graphene structures

Graphene was modeled as a two-dimensional layer with surface conductivity as given by the Kubo formula. The fermi level of graphene was selected as 0.4 eV and the relaxation time was selected as 0.35 ps, these values were selected as reasonable approximation based on previous works with CVD graphene with 1000 cm^2/V-s mobility, 0.25-0.50 ps relaxation time and fermi levels of 0.3-0.5 eV [43, 44]. The graphene ribbon of width 1.5 μm and length 6.0 μm was simulated and the same ribbon dimensions were transformed into 3D halfway and completely curved nanocylinder geometries. The LSPR frequency was simulated and the corresponding electric field enhancement was plotted. When the 2D graphene ribbon (Supporting Information Figure S2b) is self-curved (Supporting Information Figure S2c, d, e), the plasmon resonant frequency shifts to a higher frequency proportional to the change in length in the direction of polarization of the incident electric (E) field (Supporting Information Figure S2a). The simulations with a silicon substrate were carried out for a substrate of width 3μm, thickness 1.5 μm, and length 4.5 μm. The refractive index for silicon was set to 3.48. The color maps showing near-field enhancement (Figure 4) were plotted along imaginary cut planes at different positions in the 2D and 3D graphene nanostructures, captured with a 45° tilted angle (Figure 4e-h) and at two different perpendicular side views (Figure 4i-l, Supporting Information Figure S5a-d). In order to confirm that the two orders of magnitude change in the field enhancement of the 2D ribbon was caused by substrate-induced losses, simulations were carried out with substrate refractive index set to 1 for vacuum and 3.48 for silicon. The electric field enhancement (Supporting Information Figure S7b) plotted at the resulting geometrical resonant frequency (Supporting Information Figure S7a) clearly shows that the two order of magnitude change is

solely caused by the interfacial dielectric properties (refractive index) as all the other parameters were maintained to be a constant. The volumetric field (Vm^2) was computed by taking the volume integral of the near-field enhancement inside the partially and fully curved cylinders. In the case of 2D ribbons, volumetric enhancement was computed taking the thickness of an imaginary air box of the same volume as that of the completely curved nanocylinder. The volumetric enhancement was computed as the square of the ratio of the volumetric field in the presence of graphene to the incident volumetric field for the same volume. The fluctuations in the Figure 4m-o are caused by two reasons, firstly, due to the weaker mesh which fails at the free-standing graphene edges in 3D simulations. Most simulations for graphene are performed using 2D mode in comsol so do not have a non-meshed volume. Secondly, the data is extracted at every 5 nm along the perimeter of graphene but the equation of the circle coordinates and the radius of the cylinders is a non-terminating decimal ($1500/2\pi$) causing comsol to round off the circular coordinates to nearest whole number; thus, introducing further noise in the extracted results. In an attempt to provide a lower fluctuation data, simulations were carried out with a denser mesh. The finer mesh simulations were carried out in 2D mode due to limits of even supercomputing resources (Figure S8a). It is easy to see from the figure that there are significantly lesser fluctuations along the perimeter of the structures, although there is a change in the values of the near-field enhancement due to lack of longitudinal modes.

4. Simulation setup for 2D and 3D graphene structures

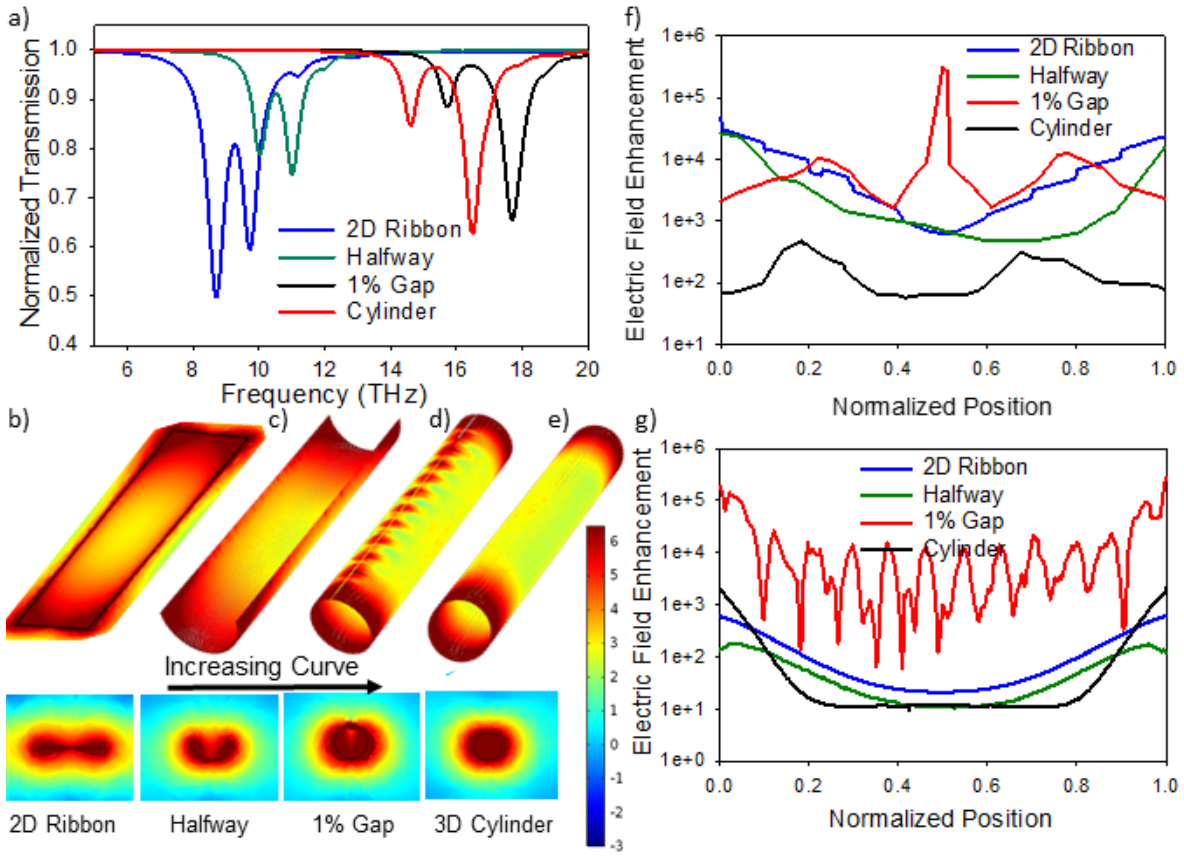

Figure S2. Simulation results of 2D and 3D graphene structures in vacuum. a) The normalized transmission through the structures. The self-assembly process causes a frequency shift in the resonance peak. b) Field enhancement plotted on the surface and cross-sectional planes for b) 2D ribbon, c) half-way curved cylinder, d) 1% gap cylinder, and e) completely curved 3D cylinder are simulated, showing the effect of geometry on field distribution and enhancement in graphene. f) Comparison of the field enhancement along the cross-sectional edge of the structures shown in c. g) Comparison of the field enhancement plotted at the center and along the length of the 2D ribbon and the 3D partially and completely curved structures. The normalized position is taken across the length and width of the structures similar to Figure 4.

5. Simulation results for the 2D and 3D graphene structures on a silicon substrate

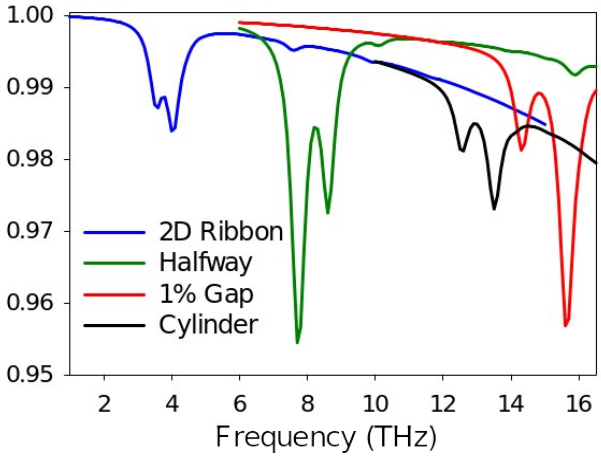

Figure S3. Transmission response for the 2D ribbon and 3D curved graphene cylinder on silicon substrate showing the geometric resonant frequency for each of the structures.

Figure S4. a-d) Near-field enhancement plotted on the surface of the 2D ribbon and on an imaginary plane placed at the center of the cross-section of the cylindrical 3D structures. e) Plot showing the actual field enhancement throughout the length of graphene plotted at the geometrical center of each of the structures along the direction denoted by the black arrow.

Figure S5. a-d) The cross-sectional images show the field enhancement in the YZ plane when the imaginary cut plane is placed at the center of the 2D and 3D structures. The field enhancement is plotted along an imaginary cut plane e) on the surface of the ribbon, f, g) at the surface of the gap created within the halfway folded and 1% gap cylinder, and h) at the surface of the completely curved cylinder along an imaginary edge.

Figure S6. a-d) The field enhancement at the center of the ribbon and cylinder through the entire length of the structures are simulated and plotted. e) The corresponding values of the volumetric field enhancement are plotted for the entire length of the structure where the volumetric field is calculated by volume integrals of the field inside the 3D structures and for an imaginary rectangular box of thickness 120nm placed on the 2D ribbon. The length for volumetric calculation is increased in intervals from 100 nm to 6 μm.

6. Comparison of the 2D ribbon on a vacuum v/s silicon substrate

Figure S7. a) Transmission response for the 2D graphene ribbon with substrate set as vacuum (black line) and silicon (red line). b) Graph showing the change in electric field enhancement across the width of the 2D ribbon with normalized position taken same as Figure 4m showing the two order of magnitude reduction on silicon (red line) compared to the enhancement in vacuum (black line).

7. Impact of self-curving on the relaxation time

The change or any deterioration in graphene properties as a result of self-curving was also simulated to find the change in the resulting near-field enhancement. The higher I_D/I_G ratio in halfway (0.357) and completely (1.063) curved nanocylinder as compared to pristine graphene (0.058) can be attributed to two factors, firstly, the strain induced in graphene as a result of the curvature, and secondly, due to edge defects induced after self-curving [2]. However, it is difficult to estimate the percentage contribution of both these factors, nevertheless it is important to note that this level of defect ratio is still considered to the in the low defect regime that extends to all Raman peak ratios below 3.0 [2]. Here, we account for the worst-case scenarios for the high I_D/I_G ratio in the 3D curved nanocylinders. The defect concentration (n_D) in graphene can be related to the Raman peak ratios using the relation below [3].

$$n_D\left(cm^{-2}\right)=\frac{(1.8\pm0.5)\times10^{22}}{\lambda_L^4}\left(\frac{I_D}{I_G}\right)$$

where, λ_L is the wavelength of Raman light source and I_D and I_G are the intensities of the D and G band peaks, respectively. The defect concentration is inversely proportional to the relaxation time; thus, all other factors remaining constant (including ~~fermi~~ Fermi velocity and ~~fermi~~ Fermi energy), this gives a 5.45% decrease in the relaxation time for the curved cylinders. However, the relaxation time and ~~fermi~~ Fermi energy do not remain constant in strained graphene. For a graphene with 10% strain, the ~~fermi~~ Fermi velocity decreases by 15% [4]. The strain in graphene can open a bandgap and also increase the bandgap in doped samples with some works even reporting an increase in work function of 0.6 eV, however, there isn't a consensus on the percentage increase in the band gap with strain [5]. It is well-known that the relaxation time (τ) in graphene can be calculated by the equation given below [45, 46].

$$\tau = \frac{\mu \hbar \sqrt{n\pi}}{e v_F}$$

where, μ is the electron mobility (2700 cm^2/V-s), $\hbar$ is the Planck's constant n is the electron density (required for a band gap of 0.4 eV chosen in our simulations), e is the charge on an electron, and v_F is the Fermi velocity (typically 1×10^6 m/s). Using these values, we obtain the relaxation time for our 2D graphene ribbons to be equal to 0.101 ps (as opposed to 0.35 ps chosen previously). With the 15% increase in fermi velocity for strained graphene the relaxation time increases to 0.118 ps. Now, if we attribute majority of the D band to defects introduced in graphene and not lattice stress, then the relaxation time for the curved nanocylinders turns out to be 0.015 ps. Simulations with a highly dense mesh compare the effect of relaxation time on the near-field enhancement in the 2D ribbon and 3D cylinders (Figure S8b). The results show that the spectral width for the plasmon peaks in ribbon and cylinder is nearly 11.71 and 10.69 THz, respectively. Moreover, even with the reduced relaxation time and in the absence of a conducting silicon substrate, the 3D cylinders demonstrate a volumetric enhancement that is 4 times stronger than the volumetric enhancement obtained for ribbons (assuming a thickness over the ribbon to make the volume equal to the volume within cylinders). Furthermore, high surface quality of the Al_2O_3 layers is critical to the plasmons induced in graphene. Previous results show that when a dielectric material such as some spin-coated polymers or e-beam evaporated aluminum oxide are in contact with 2D and 3D graphene they seek to shift the resonant frequency proportional to the refractive index but do not significantly alter the near-field enhancement [47]. It is important to note that the folding mechanism introduced here is not limited to CVD graphene or Al_2O_3 protection layers. Graphene cylinders can also be fabricated using mechanically exfoliated graphene with hBN layers added between the current Al_2O_3-Graphene interfaces that have shown

to also increase the relaxation to 3 ps [48]. The aluminum oxide can also be replaced with other suitable materials such as SiO_2, or CaF_2.

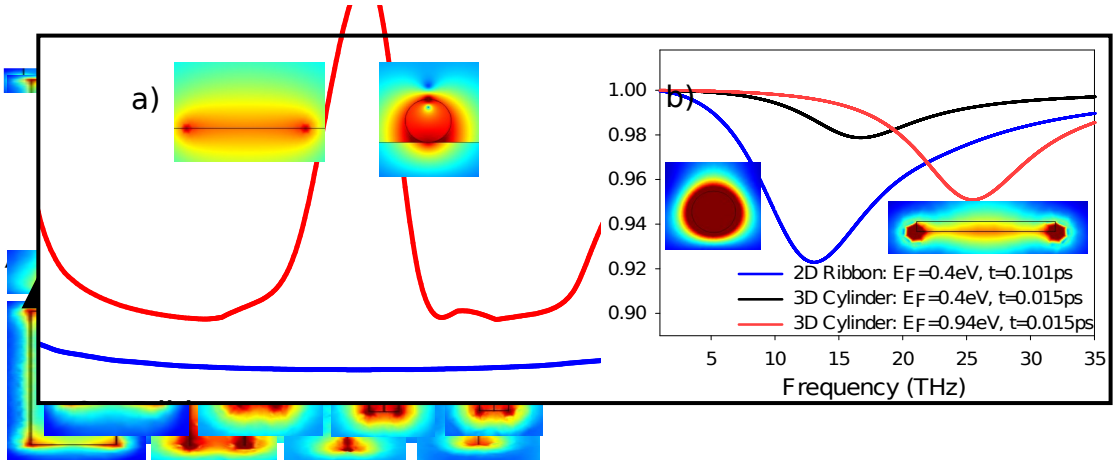

Figure S8. a) Near-field enhancement plotted along the width of the ribbon and the circumference of the 3D cylinders with 1% gap under 2D simulations with a dense mesh to reduce any noise and fluctuations. b) Transmission response showing the effect of change in relaxation time and fermi level on the plasmon resonance caused due to curving of the 2D graphene into 3D completely curved cylinders. The insets show the corresponding near-field enhancements.

8. SINS-based characterization of the plasmon resonance in 3D nanocylinders

The AFM height data shows the morphology (thickness) of the self-assembled graphene cylinders (Figure 5a, Supporting Information Figure S9a). The gap within the cylinder structures is below 15 nm as evident from the SEM images in Figure 2, however, due to the convolution of the tip radius (~25 nm), a larger gap of nearly 60-100 nm is perceived from the AFM data. The 3nm alumina layer used to support and protect the graphene is thin enough for the AFM tip to measure optical properties of the underlying graphene. The broadband infrared white light images are integrated across the detector bandwidth, approximately 330-1400 cm^{-1}. The images collected for different areas of the same sample show the strong edge-scattering in the 3D graphene cylinders (Supporting Information Figure S9b). The rough surface of the silicon substrate adds to the noise level but the ~~absorption~~ scattering on the 3D graphene remains clearly visible. The non-uniformity in the mapped images on the graphene cylinders is primarily caused by the cracks and voids in the pristine graphene grown on the copper foil and non-uniformity of the chemical doping process. The white-light amplitude along 4 different positions as shown in (Supporting Information Figure S9c) was extracted using Gwyddion. The line profiles clearly demonstrate higher signal on the graphene surface, which extends from about 0.1μm to 1.1μm in the graphed line profiles (Supporting Information Figure S9c). It should be noted here that the actual diameter of the graphene cylinders is much smaller than the perceived diameter, which is a convolution of the tip radius and the sample size~~, but the tilt of the sample gives a higher perceived diameter~~. The perfect overlap of the actual AFM topography with the near-field ~~absorption~~ scattering images prove that the graphene-based enhanced ~~absorption~~ plasmon performance that is observed is not an artifact or due to the underlying substrate (which is several

100nm away much farther than SINS vertical resolution). The plasmon wavelength is measured as twice the spectral distance between successive fringes in the ~~absorption~~ scattering data profile. ~~The synchrotron light is broadband source, thus, it cannot be exactly determined that the integrated absorption images correspond to exactly what frequency. To determine the exact frequency causing the strong absorption, spectra is collected using line scans over a few different positions on the cylinder structure. Spectra demodulated at the~~ The second and third harmonic deflection ~~tapping frequency of the AFM tip of the cantilevers are considered tprovide the best compromise between near-field sensitivity while o be optimum for measuring the near-field while maintaining a highgood signal to noise ratios (SNR).~~ The ~~captured~~ acquired ~~spectrum~~ spectra at the second and third harmonic tapping frequency of the AFM tip (Supporting Information Figure S9d) shows a clear increase in amplitude for the range ~~of 600-700 cm^{-1}~~ when measured on the cylinder surface. The spectrum also demonstrates the nearly flat and low ~~absorption~~ scattering signal in this frequency regime when measured on the silicon surface that exists between the graphene cylinders. Thus, the spectrum proves that the measured increased ~~absorbance~~ scattering is due to the graphene 3D structure and not an artifact. ~~Confinement factor is then calculated as the ratio of incident synchrotron wavelength to the plasmon wavelength. It should be noted here that in the simulated samples a 5 orders of magnitude enhancement occurs at the center of the longitudinal split gap within the cylinders (Figure 4m), however, as seen in the measured profiles (Figure S9c), a similar increase occurs at all three positions. This is a limitation of the AFM-IR process such that only absorption on a film can be measured and absorption inside the small gap cannot be probed the AFM tip morphology. Due to these limitations, currently the measurement of the cross-sectional enhancement in the 3D cylinder openings continues to be a challenge even with the advantages of the SINS technologies. Even~~

~~with this limitation, the measurements also demonstrate the advantage of the 3D graphene cylinders in terms of high substrate compatibility and ease of integration.~~

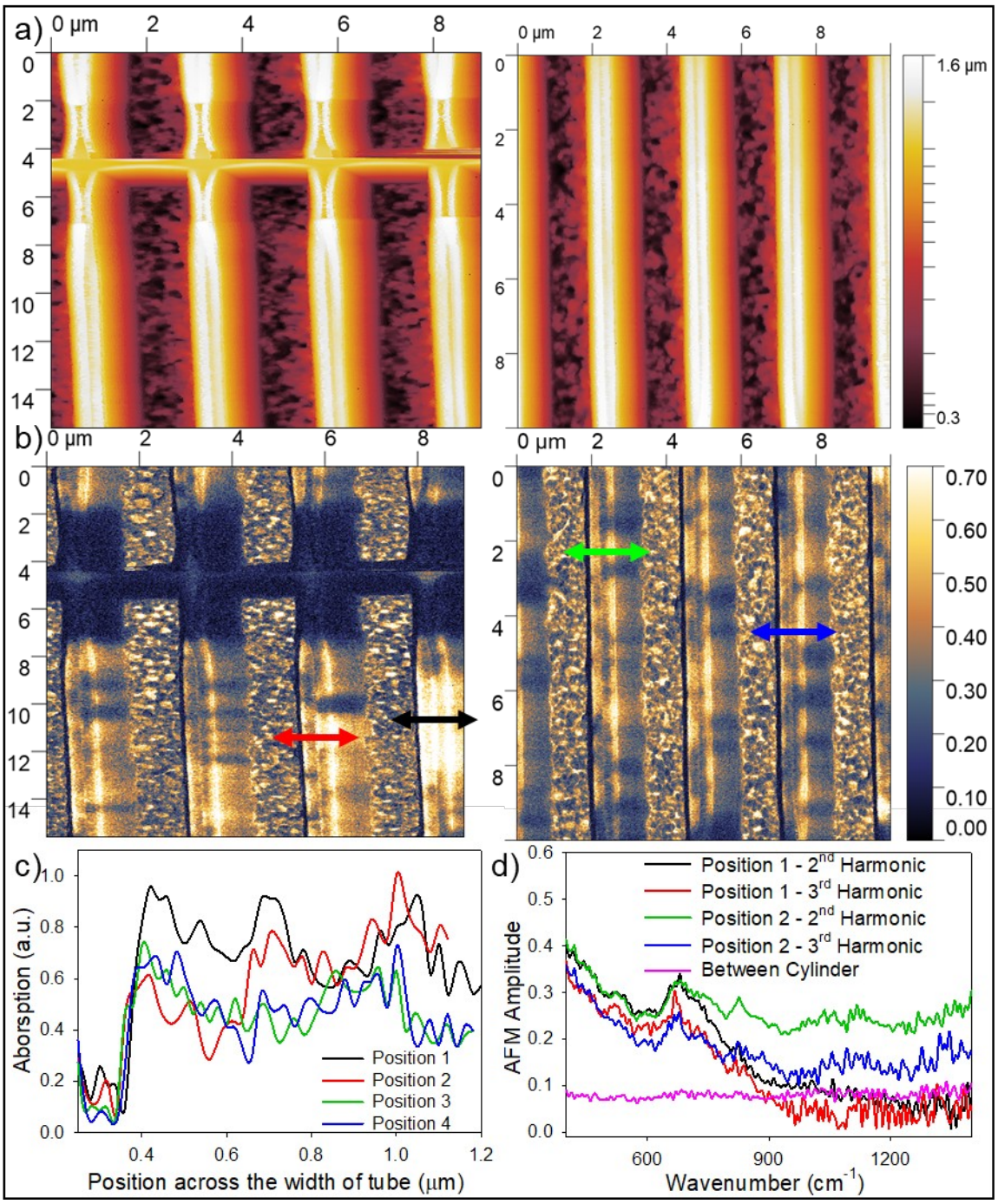

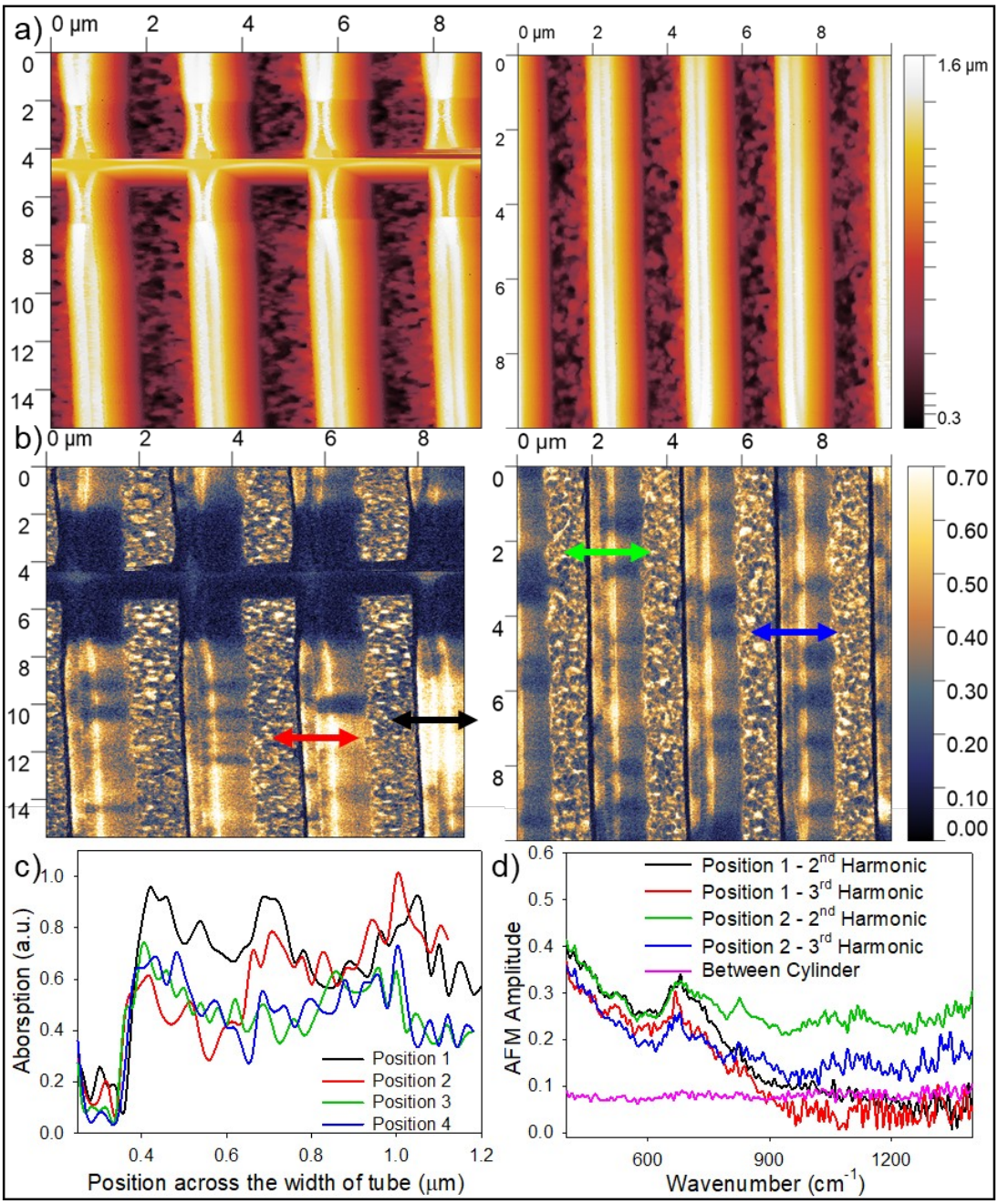
a)
0 µm
2
4
6
8
1.6 µm
0.3
b)
0.70
0.60
0.50
0.40
0.30
0.20
0.10
0.00
c)
Aborsption (a.u.)
Position 1
Position 2
Position 3
Position 4
Position across the width of tube (µm)
d)
AFM Amplitude
Position 1 - 2nd Harmonic
Position 1 - 3rd Harmonic
Position 2 - 2nd Harmonic
Position 2 - 3rd Harmonic
Between Cylinder
Wavenumber (cm-1)

Figure S9. SINS data measured for the 3D graphene cylinders. a) AFM topography images showing the thickness and curvature of the cylindrical graphene samples. b) AFM amplitude data corresponding to the near-field on the graphene and silicon surfaces. c) Actual AFM amplitude data corresponding to the graphene ~~absorption~~ scattering acquired for various positions as shown in b. d) Second and third harmonic line scan spectra for the graphene cylinders captured for various positions on the sample.